Natural Resources
Canada

Ressources naturelles
Canada

GEOLOGICAL SURVEY OF CANADA
OPEN FILE 8233

3-D modelling of magnetotelluric data from the Abitibi and Pontiac subprovinces of the Superior Province, Ontario and Quebec

E. Roots and J.A. Craven

2017

Celebrating 175 yrs

Canada

GEOLOGICAL SURVEY OF CANADA
OPEN FILE 8233

3-D modelling of magnetotelluric data from the Abitibi and Pontiac Subprovinces of the Superior Province, Ontario and Quebec

E. Roots and J.A. Craven

2017

Recommended citation
Roots, E. and Craven, J.A., 2017. 3-D modelling of magnetotelluric data from the Abitibi and Pontiac Subprovinces of the Superior Province, Ontario and Quebec; Geological Survey of Canada, Open File 8233, 24 p. doi:10.4095/300666

Introduction

Magnetotelluric geophysical exploration comprises the measurement of time-varying fluctuations of the natural electric and magnetic fields of the Earth (Cagniard, 1953; Tikhonov, 1950). Data from multiple sites spanning a survey area are analyzed in the frequency domain and used to map the spatial variation of the subsurface electrical properties (i.e. the resistivity). In the frequency domain a skin effect controls the depth of investigation and for simple layered earth structure (1-D) signals with longer periods (or lower frequencies) penetrate to deeper layers than shorter periods (or higher frequency) signals. If a broad range of frequencies at each site are measured then the variation of resistivity with depth can be determined.

Enhanced electrical conductivity (the inverse of resistivity) in the crust is often linked to the presence and mobility of charges within a variety of material: aqueous fluids within porous strata (e.g., Glover and Vine, 1995; Hyndman et al., 1993), graphite, interconnected grains of metallic oxides, and sulphides, (e.g., Jones and Craven, 1990; Katsube and Mareschal, 1993; Li et al., 2003). Laboratory studies have indicated there are several sources of enhanced electrical conductivity in the mantle, including graphite, hydrogen, partial melt, water, and temperature variation (e.g., Constable, 2006; Ducea and Park, 2000; Hirth et al., 2000; Jones, 1999; Karato, 1990; Korja, 2007; Selway, 2013; Yoshino et al., 2008). The spatial variation of the resistivity can also be used to infer processes that have led to the formation and subsequent modification of a region (e.g., Evans et al., 2011; Ferguson et al., 2012; Spratt et al., 2009).

Much has been written about the Superior Province and therefore only a cursory summary will be presented here. It largely consists of rocks formed between 2.8 and 2.7 Ga (Hoffman, 1989) ago. The recent study area is largely focussed on the Abitibi Subprovince whose characteristic polycyclic volcanic stratigraphy is overlain by a sequence of turbiditic sedimentary material and synorogenic clastic rocks. The Abitibi is thought to be a remnant of a larger Neoarchean granite–greenstone terrain that underwent rapid crustal growth during the Neoarchean (Card, 1990; Percival et al., 2004) . Several periods of granitic intrusion and folding and faulting also characterize the Abitibi Subprovince (Card and Poulsen, 1998). The study area also includes the Pontiac Subprovince, an Archean metasedimentary (and plutonic) terrane separated from the Abitibi to the north by the Cadillac Larder– Lake Fault Zone (CLLFZ) (see Figure 1). The boundary of the Abitbi subprovince with the Grenville

Province to the south is marked by the Grenville Front Tectonic Zone (GFTZ) (Card and Ciesielski, 1986).

The magnetotelluric data used in this study are described in detail in Boerner et al. (2000) and Adenunji et al. (2014) who have redone the 2D modelling in the region. This report is focussed on generating new 3-D maps of the spatial variations, and compares the result with previous models for the area.
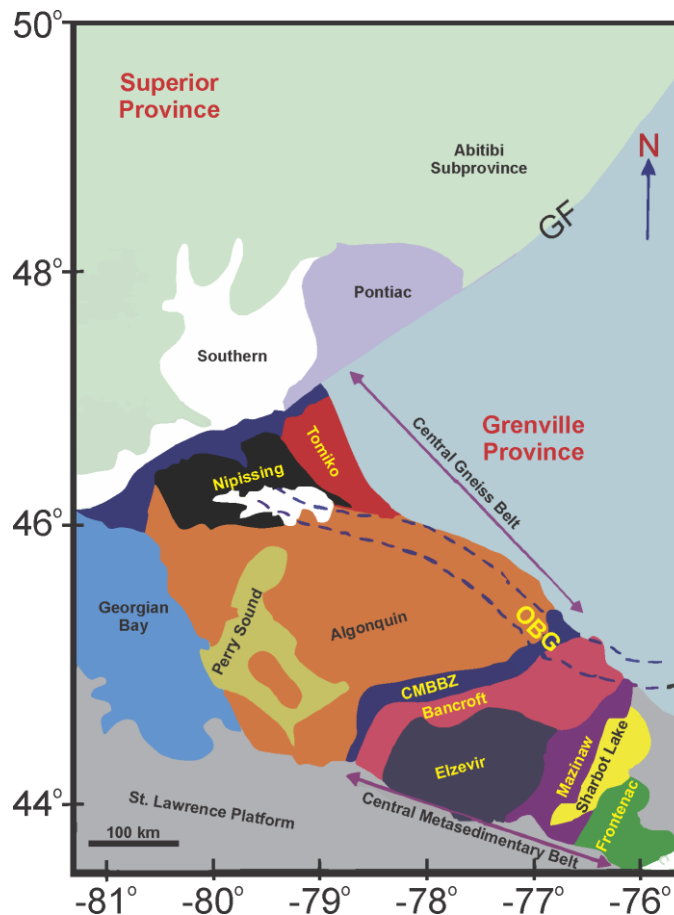

Figure 1: Simplified geotectonic map of the study area. Sub-units of the Superior and Grenville Provinces are labeled. GF = Grenville Front, OBG = Ottawa Bonnechere Graben; CMBBZ = Central Metasedimentary Belt Boundary Zone. Modified after Adetunji et al. (2014).

Data Selection

Full impedance tensor data was available at 129 sites, while vertical field transfer function data of varying quality was available at 97 sites. The data that was collected contains periods ranging from 0.0026 s to 1820 s. Inversion of a large number of sites across a broad frequency band requires a

significant amount of computer memory, and so the first step in the inversion process is data selection. A preliminary model and dataset was built using all 129 sites, and the data sensitivity matrix was calculated for a half-space model with a resistivity of 10000 Ω-m. Using the sensitivity matrix in combination with visual inspection of the data, 24 sites were removed from the dataset. Sites were removed on the basis that they were generally within a few kilometers of other sites, and as such had very similar data and overlapping ranges of sensitivity. Next, the periods to be inverted were selected. The data tended to be have higher associated errors at the lowest and highest periods, and were therefore excluded. A total of 14 periods were selected between 0.01042 s and 1365 s, with 2 or 3 periods per decade. Finally, while the majority of the sites include transfer function data, we were forced to exclude it from the inversion due to computational restrictions.

3-D Modelling

Data was inverted using the WSINV3DMT modelling code (Siripunvaraporn et al., 2005). The code uses the Occam approach which seeks a model with minimum structure and appropriate fit to the provided data. Orienting the mesh and data with geological structure is useful when the diagonal components of the impedance tensor are not being inverted (Kiyan et al., 2014). Nonetheless, in order to simplify interpretation, the mesh and data azimuths were set to 0˚ and all impedance components were included in the inversion. The diagonal (Z_{xx} and Z_{yy}) components tend to have higher associated errors than the off-diagonal components, and so are typically down-weighted in the inversion process. This down-weighting takes the form of increasing the associated errors. If the errors are increased by a large factor, the inversion process practically ignores the diagonal components d this has been shown in synthetic studies by Kiyan et al. (2014) to lead to erroneous results. In order to strike a compromise between being able to match all the data without overfitting to noise, the errors associated with the diagonal components were increased by a factor of 10, and an error floor of 7.5% was applied to all components.
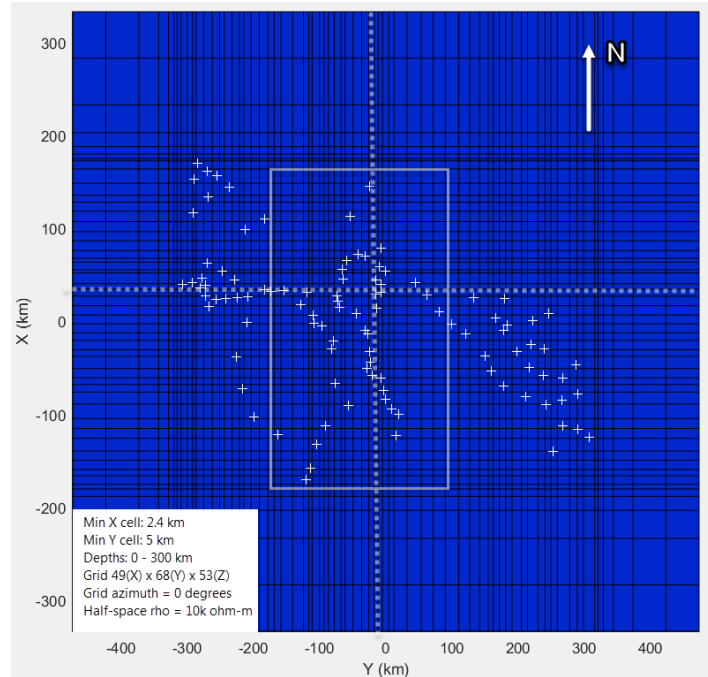
Figure 2: Initial model used for inversion. '+' signs indicate site locations. White dashed lines indicate positions of the depth slices shown in Figure 3. The solid rectangle indicates the bounds of model resulting from the focused inversion.

The inversion process attempts to find the best fitting model while also minimizing the difference between successive iterations and the starting model. It has been found that when starting with a half-space model the inversion tends to converge to a local minimum in terms of RMS misfit within a few iterations (typically 3 to 5). In most cases however, the RMS of the best fitting model among these iterations is unsatisfactory. It has been found that superior results may be attained by taking the best fitting model among the initial iterations, and restarting the inversion using it as the starting model. Note that some caution should be exercised when doing this. A starting model with geologically impossible features will tend to generate further iterations with impossible features, albeit with a lower RMS misfit.

Beginning with a half-space model (Figure 2), the inversion was run for 3 iterations. The best fitting model among these was then set as the starting model, and another 3 iterations were run. This process was repeated a total of 7 times, eventually reaching a model whose response fits the data with an RMS of 2.136.

Figure 3 shows a collection of depth slices, and Figure 4 shows west-east and south-north slices (profiles shown in Figure 2). The top 10-20 km of the model is generally resistive, with values exceeding 10000 Ω-m. In most parts of the model, there is a transition at around 10-15 km from the resistive upper crust to more conductive layers which persist down to mantle depths. Beyond these

large scale features, the model is marked by a number of small, isolated conductors at depths less than 10 km. While the range of periods included in the inversion should be sufficient to resolve some structure at depths shallower than 10 km, the discontinuity of the shallow conductors in the vertical direction suggests that more mesh is required between 5 and 10 km. At depths greater than 20 km, the model is spotted with several conductors, some of which connect with conductors at greater depth (C2, C5), and others which terminate within a few layers (C1, C3, C4).
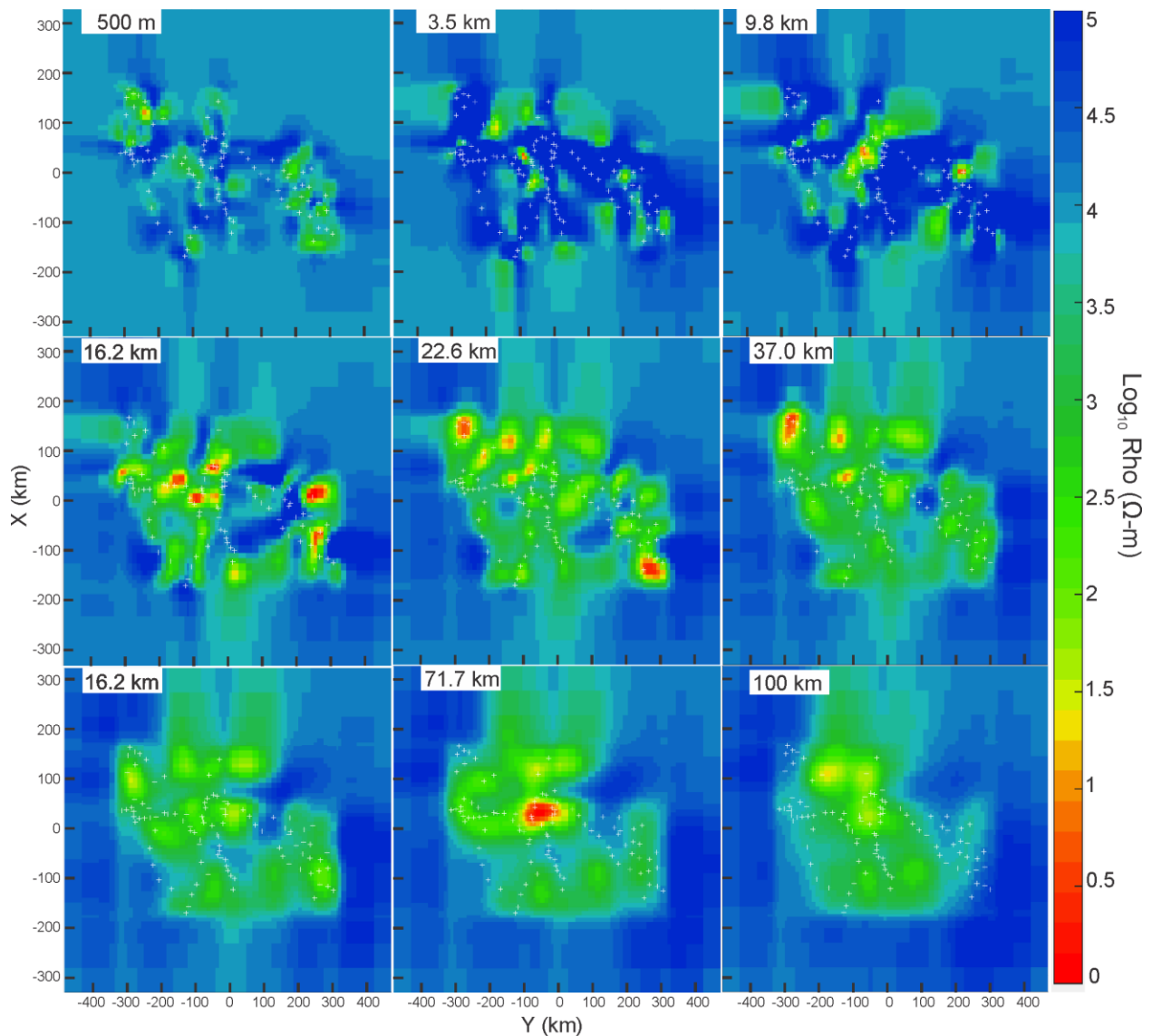

Figure 3: Plan views of the model at various depths.

In general the MT method is better at resolving conductors than resistors (Smith and Booker, 1988). It is often difficult to interpret whether or not a resistor is present in a model because the data requires it, or simply because of the choice of regularization combined with lack of sensitivity to that region. To

attempt to quantify the relative uncertainty associated with different features of the final model, the resolution matrix for the model was calculated following a method similar to that given in Grayver, (2013). Starting with the sensitivity matrix $\mathbf{J}$, a data-weighted sensitivity matrix is calculated via

$$\bar{\mathbf{J}} = \mathbf{W}_d \mathbf{J} \in \mathbb{C}^{N_d \times N_m} \tag{1}$$

where $\mathbf{W}_d$ is a diagonal matrix whose diagonal elements correspond to the inverse of the data errors. The sensitivity matrix is an $N_d \times N_m$ matrix, where N_d and N_m are the number of data and model parameters, respectively. Note that for the inversion code used here, the real and imaginary parts of the impedance data are considered separately, and so we re-write the weighted sensitivity matrix as:

$$\hat{\mathbf{J}} = \begin{pmatrix} Re\{\bar{\mathbf{J}}\} \\ Im\{\bar{\mathbf{J}}\} \end{pmatrix} = \begin{pmatrix} \mathbf{W}_d & \mathbf{0} \\ \mathbf{0} & \mathbf{W}_d \end{pmatrix} \begin{pmatrix} Re\{\mathbf{J}\} \\ Im\{\mathbf{J}\} \end{pmatrix} \in \mathbb{R}^{2N_d \times N_m} \tag{2}$$

To calculate the resolution matrix, the right singular vectors of $\hat{\mathbf{J}}$ are required. The singular value decomposition (SVD) of $\hat{\mathbf{J}}$ is be written as:

$$\hat{\mathbf{J}} = \mathbf{U}\mathbf{\Sigma}\mathbf{V}^T = (\mathrm{U}_r \ \mathrm{U}_0) \begin{pmatrix} S_r & \mathbf{0} \\ \mathbf{0} & \mathbf{0} \end{pmatrix} \begin{pmatrix} \mathbf{V}_r^T \\ \mathbf{V}_0^T \end{pmatrix} \tag{3}$$

where the columns of $\mathbf{U}$ and $\mathbf{V}$ are comprised of the left and right singular vectors of $\hat{\mathbf{J}}$, respectively, and $\mathbf{\Sigma}$ is a diagonal matrix whose elements are the singular values of $\hat{\mathbf{J}}$. The resolution matrix is then calculated as:

$$\mathbf{R} = \mathbf{V}_r \mathbf{V}_r^T \tag{4}$$

The resolution matrix describes how well each model parameter (i.e. cell) is resolved. Ideally it is an identity matrix, representing that each parameter is perfectly resolved. However due to the fact that the inversion problem is underdetermined, in addition to the smoothing that occurs in Occam style inversions, each model parameter results from an averaging process with other nearby parameters (Alumbaugh and Newman, 2000). Each row of the resolution matrix represents a single model parameter, and the elements of that row indicate the weight each other parameter had in the averaging process. As the model resolution matrix is $N_m \times N_m$, in most cases for 3-D inversions it is infeasible to store the full matrix. Therefore, only the diagonal of $\mathbf{R}$ was calculated and stored. The resulting vector represents the weight each model parameter has in determining its own value, or in other words, the resolution of each individual model parameter.

Figure 4c and d show the same sections of the model as Figure 4a and b, but with the transparency of the model set to reflect the resolution of each parameter relative to the average cell resolution. Note that as cells with large volumes (e.g. those cells within the model padding) tend to have inflated

sensitivity values, and therefore resolution values. To counter this, the resolution of each model parameter was scaled by its volume. Cells which are completely opaque are said to be reasonably well resolved, while those that are completely transparent are poorly resolved. Consistent with the physics of the magnetotelluric method, the centers of all conductors have good resolution. The large regions of connected conductors (e.g. C2a, C2b, and C2c) also seem to be well resolved. The resistive areas which break up the conductive regions (R1, R2, and R3) are not well resolved, and so it is difficult to say whether or not there is in fact a resistive gap between the conductors.
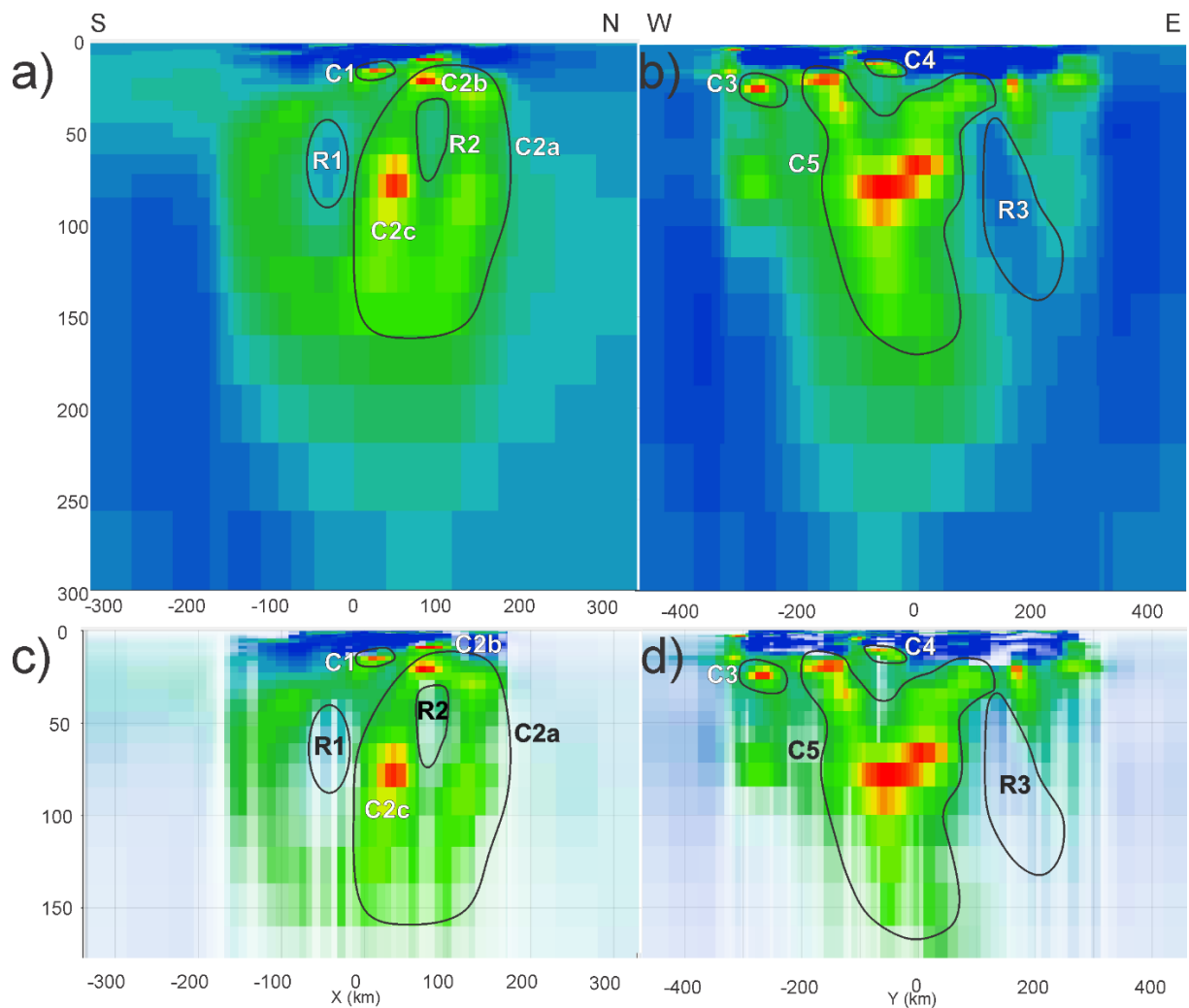

Figure 4: a) South-north and b) west-east depth slices with positions as indicated by the dashed lines in Figure 2. c) and d) show the same slices as a) and b), respectively, but with the transparency of the model cells set relative to its corresponding value in the model resolution matrix.

Data Fit

As was mentioned earlier, the RMS misfit of the model is 2.13. The RMS misfit of each of the components that were inverted are given in Table 1. The overall RMS at each site is shown in Figure 5. A number of sites near the center of the model have a higher than average RMS. The highest misfit is found at site g90010, with an RMS of 5.7. Figure 6 shows a set of determinant average apparent resistivity pseudo-sections at 4 periods. These sections were generated by calculating the apparent resistivity at a number of periods for each site, and then applying a natural nearest neighbor interpolation scheme (Sibson, 1981) The general trend of these sections is matched by the generated model, namely higher resistivities at lower periods (shallower depths), moving to lower conductivity with increasing periods (i.e. depth). Overall, apparent resistivity pseudo-sections generated using the model response (Figure 7) match well with those generated using the raw data. One feature of these data pseudo-sections that is not recovered in the model nor the response pseudo-sections is the resistive feature near the center of the model ('R' in Figure 6). Note that the anomalously high apparent resistivity is due to the data at site g90010 (data for this and other sites are shown in Figure 8, 9, and 10), which explains the poor data fit at that site.

Table 1: RMS misfit for each data component

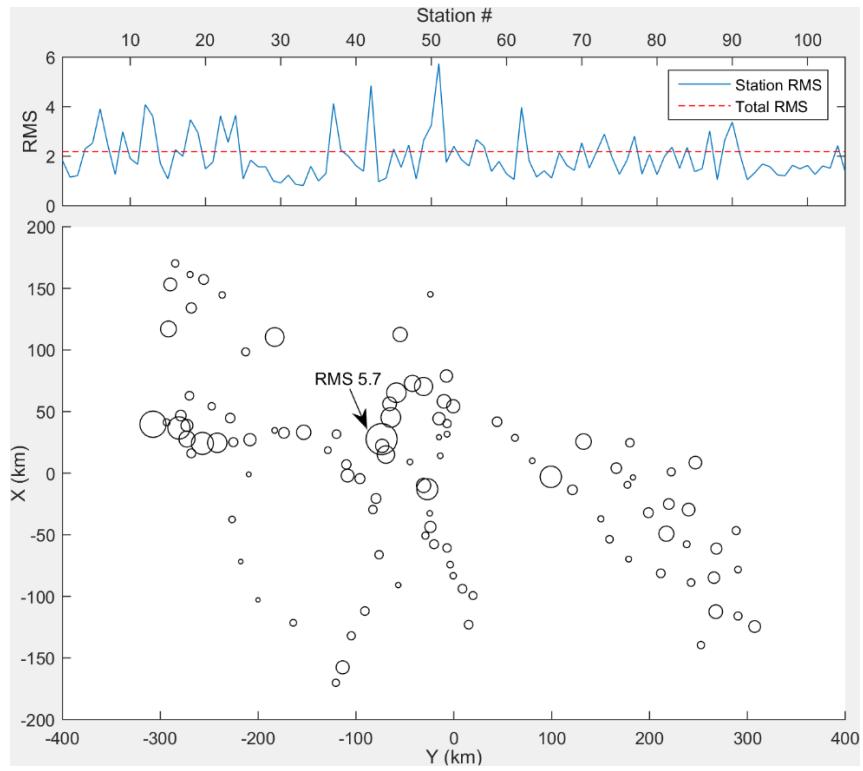| Component	Base Error Multiplier	RMS Misfit
ZXXR	10	1.5
ZXXI	10	1.87
ZXYR	1	2.21
ZXYI	1	2.67
ZYXR	1	2.21
ZYXI	1	2.61
ZYYR	10	1.88
ZYYI	10	2.27

Figure 5: Top – RMS misfit for each site that was used in the inversion. Bottom – Map of the sites, where the size of each circle indicates the relative data misfit at each site. The site with the largest RMS (g90010) is indicated by the arrow.
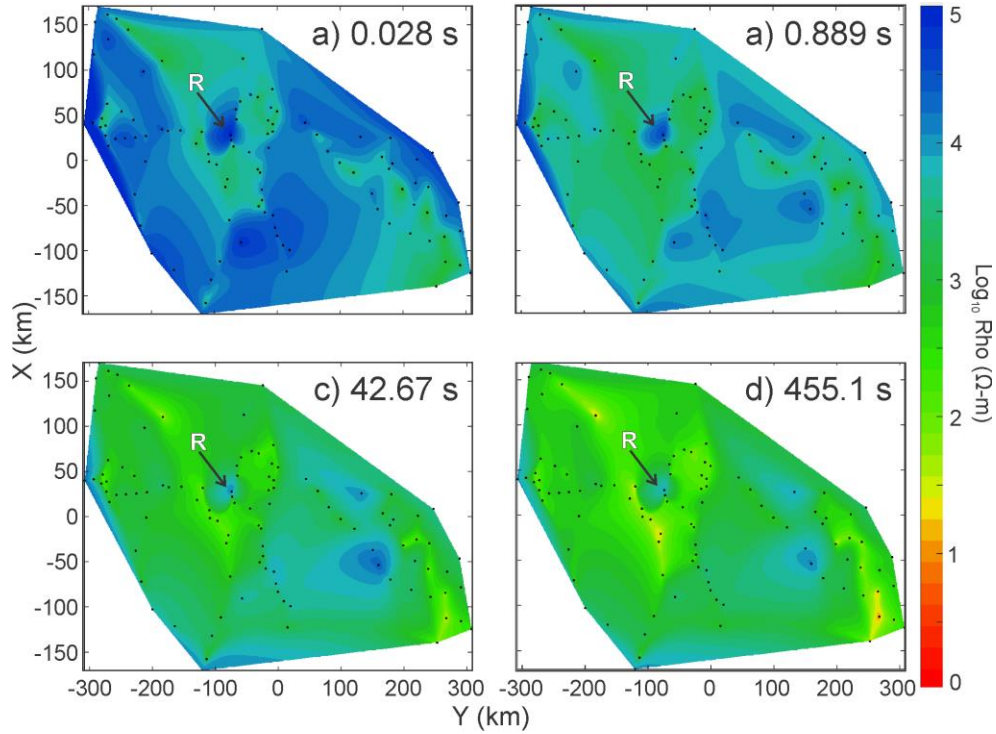
Figure 6: Determinant average apparent resistivity sections generated using the data at periods of a) 0.028 s, b) 0.889 s, c) 42.67 s, and d) 455.1 s. Values are interpolated between sites using the natural nearest neighbor interpolation scheme (Sibson, 1981).
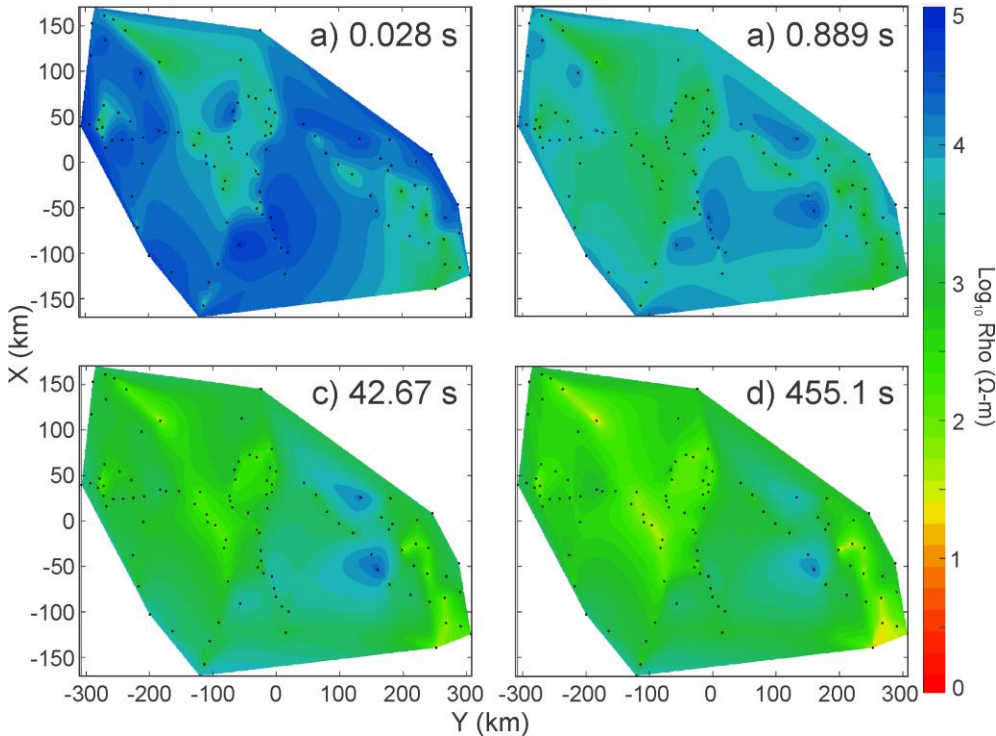

Figure 7: Determinant average apparent resistivity pseudo-sections generated using the model response at periods of a) 0.028 s, b) 0.889 s, c) 42.67 s, and d) 455.1 s.
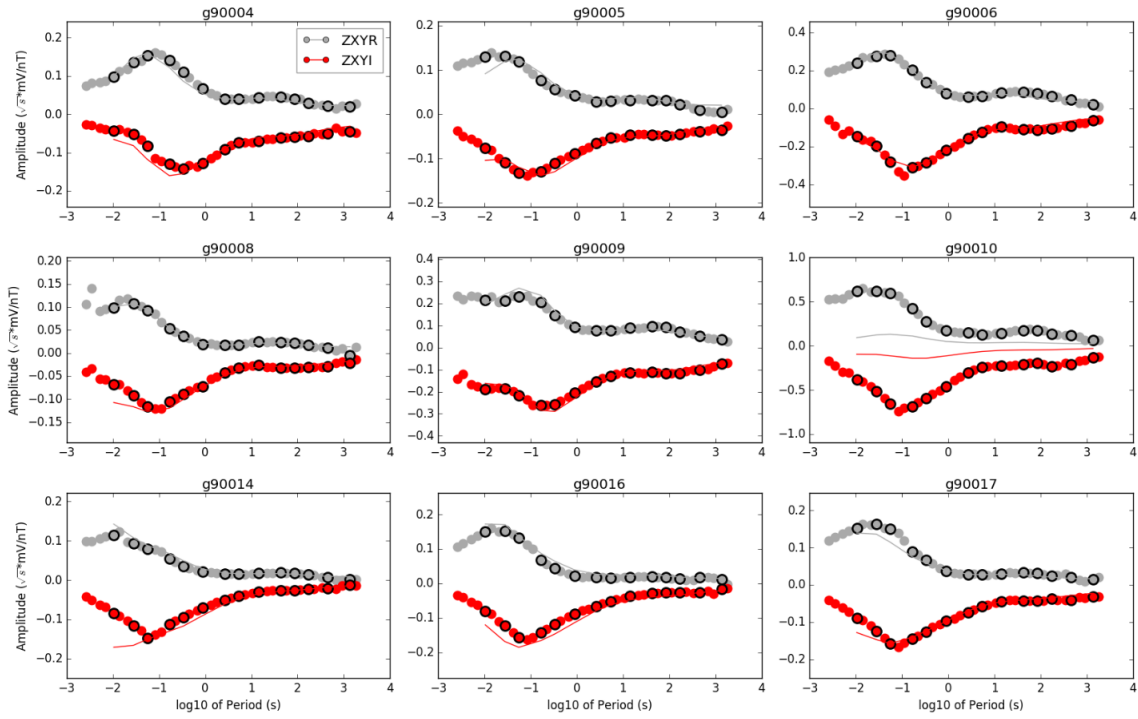
Figure 8: Data and response plots for the ZXY data components. Note the anomalously high values and poor fit for site g90010. Y-axis values are scaled by the square root of the periods. Data points that were used in the inversion are outlined in black.
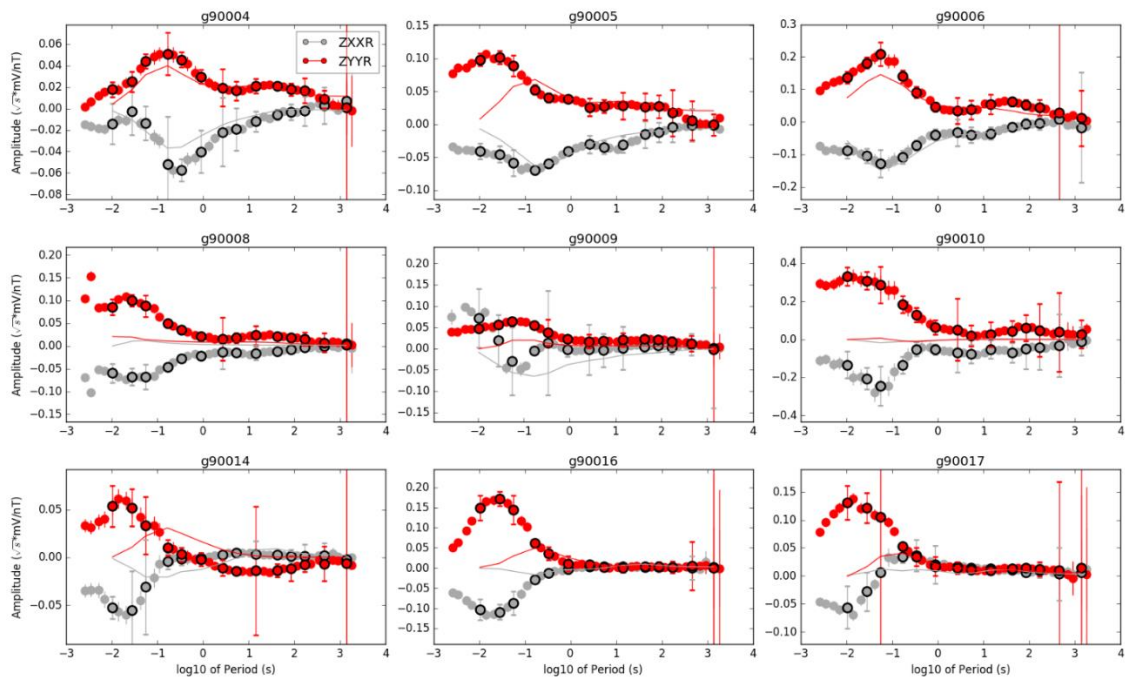

Figure 9: Data and response plots for ZXXR and ZYYR components. Amplitude values have been scaled by the square root of the period.
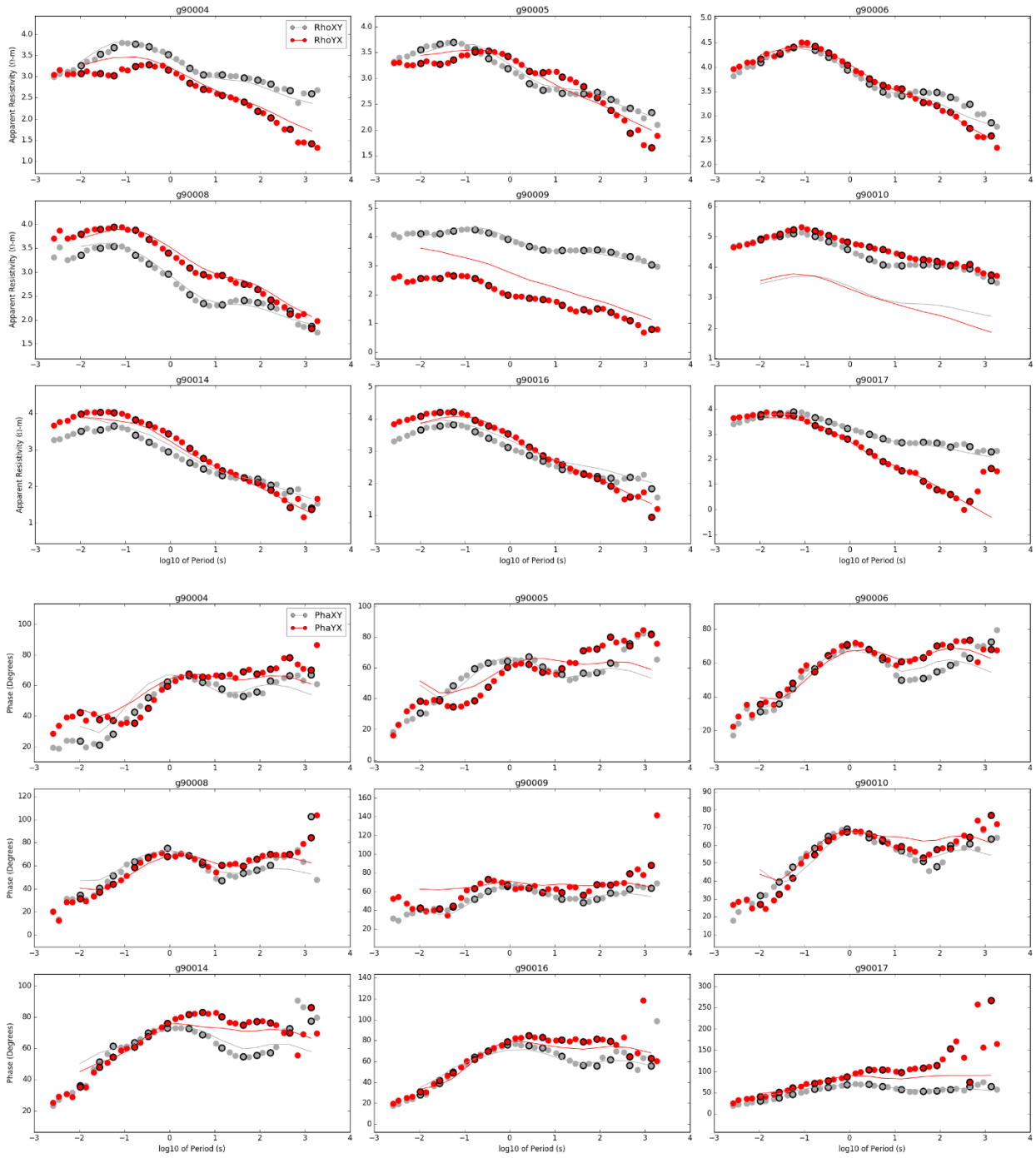
Figure 10: Data and response plots of apparent resistivity and phase. Apparent resistivity data is shown in a log_{10} scale

Focused Inversion

The large-scale features at crustal depths in the model presented above are fairly pronounced. The model suggests a highly resistive crust from 0-10 km depth for the western part of the model, with a sudden increase in the thickness of the resistive feature beginning at the part of the model which corresponds with the boundary between the Southern and Pontiac sub-provinces. However, as was discussed in the previous sections, the resolution at depths shallower than 10 km is very poor due to a combination of the mesh and periods used in inversion. Therefore, to resolve features within the 0-30 km range, a second model was generated using a much finer mesh, focusing on the central corridor of stations (white box in Figure 2) and using periods ranging from 300 to 0.1 Hz. The resulting model had an RMS of 2.56. The model presented in the previous sections, and the smaller scale model will hereafter be referred to as models A and B, respectively.

 Figure 11 shows coincident west-east cross-sections of the two models along the dashed line and constrained within the white box indicated in Figure 2. There are some obvious similarities and differences between the models that highlight one of the problems with inversions, namely that of non-uniqueness. The upper-most section of conductor C5 has been imaged in roughly the same location in both models, considering the difference in mesh size. Conductor C4, however, is located 20-30 km further east in model B. These differences suggest that in general, the small scale structures above 10 km depth in both models should be considered carefully. There are also similarities and differences in the larger scale structures within the models. The biggest difference pertains to the lateral continuity of conductor C5. The resolution of the cells beneath conductor C4 in model A is noticeably lower than that of the surrounding cells. As a result, it is difficult to say whether or not the resistive zone separating C4 from C5, as well as the gap between western and eastern portions of C5 are real. Model B brings this further into question. While there is still a zone of higher resistivity separating C4 and C5, the gap separating the western and eastern sections of C5 itself has vanished.
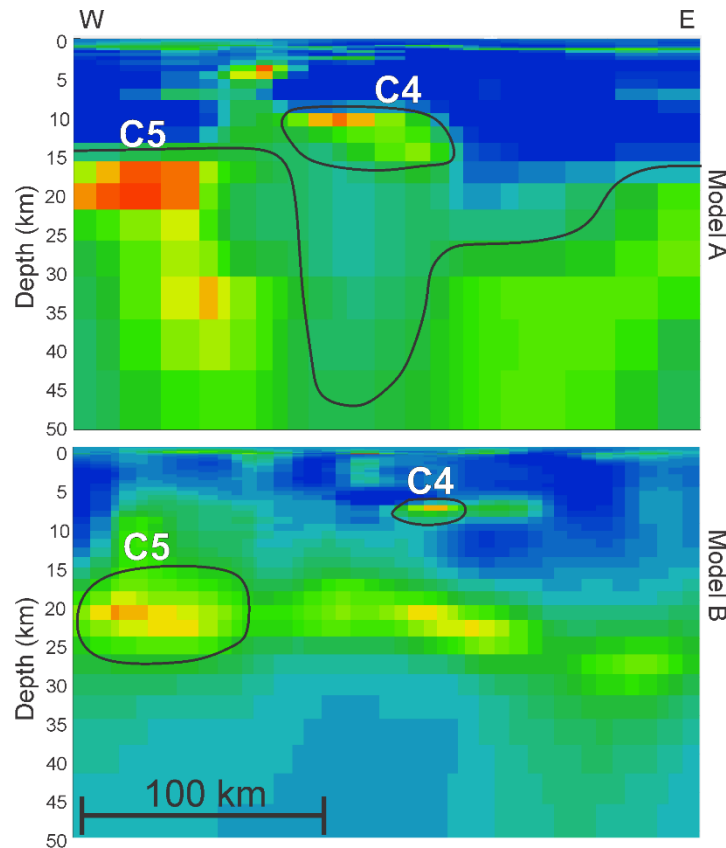
Figure 11: West-east sections of model A (top) and B (bottom) along the horizontal dashed line within the white box in Figure 2.

Rather than comparing the south-north sections of models A and B, Figure 12 shows slices from each model taken by interpolating the models between the sites along the south-north profile (see Figure 13 for the path taken). The path taken is very close to the south-north taken by the slice in Figure 3a, and some of the same features are visible in Figure 12. As was the case with the west-east sections, there are similarities and differences between this slice of models A and B. It is encouraging to see that conductor C2b is visible in both models in nearly the exact same locations. The greater resolution at shallow depths afforded by the focused model seems to agree with what is seen in model A, namely that the there is a thinning of the resistive portion of the crust in the vicinity of C2b. The models do disagree on whether or not the upper and lower portions of C2b are in fact connected. Both models have a slightly conductive feature further to the north, however they disagree as to its exact location. In model A, C2a occurs ~40 km north of C2b, while in model B this distance is nearly 100 km. Another similarity between the models as shown in these slices is the structure at depths less than 20 km. While the exact resistivity values vary, both models show features R1 and R2 as having similar

geometry, and having resistivities greater than 10000 Ω-m. Furthermore, they both agree on the increased thickness of R1 to both the south and north of C2b.
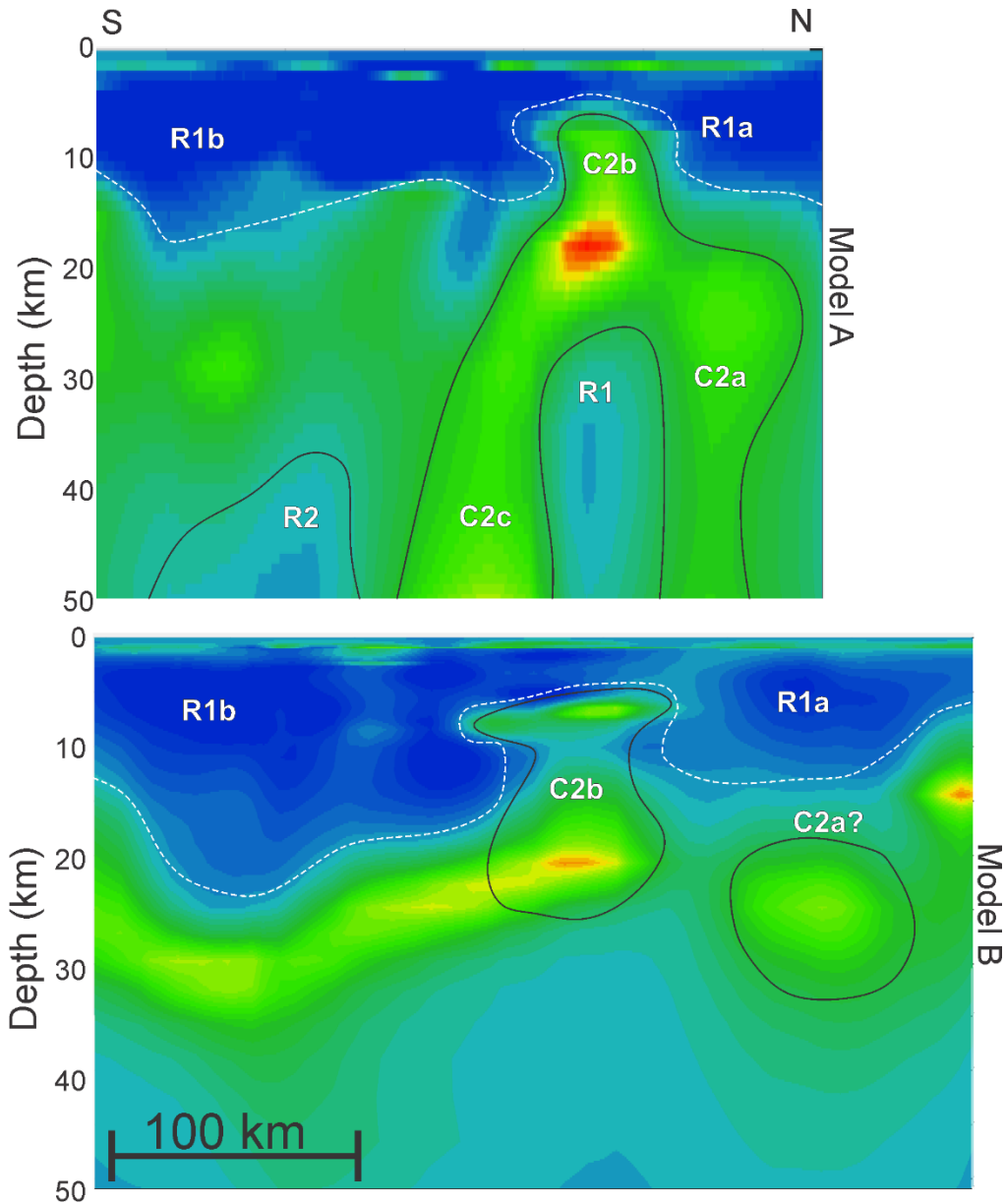

Figure 12: Slices from models A (top) and B (bottom) through a south-north profile of stations. The plots are aligned such that the lateral positions correspond to the same locations.

Comparison with 2-D results

Adetunji et al. (2014) examined and inverted apparent resistivity and phase data from 40 MT stations from the Lithoprobe and POLARIS projects along a 650 km long profile through the Abitibi-Grenville provinces. The Lithoprobe sites form part of the dataset used in this study. Figure 13 shows a map of

the region, with the site locations used in the 2-D inversion (black triangles and pentagons) and the overlapping sites in the 3-D survey (grey diamonds). The sites along the dashed white line also represent the path taken by the slices in Figure 12.
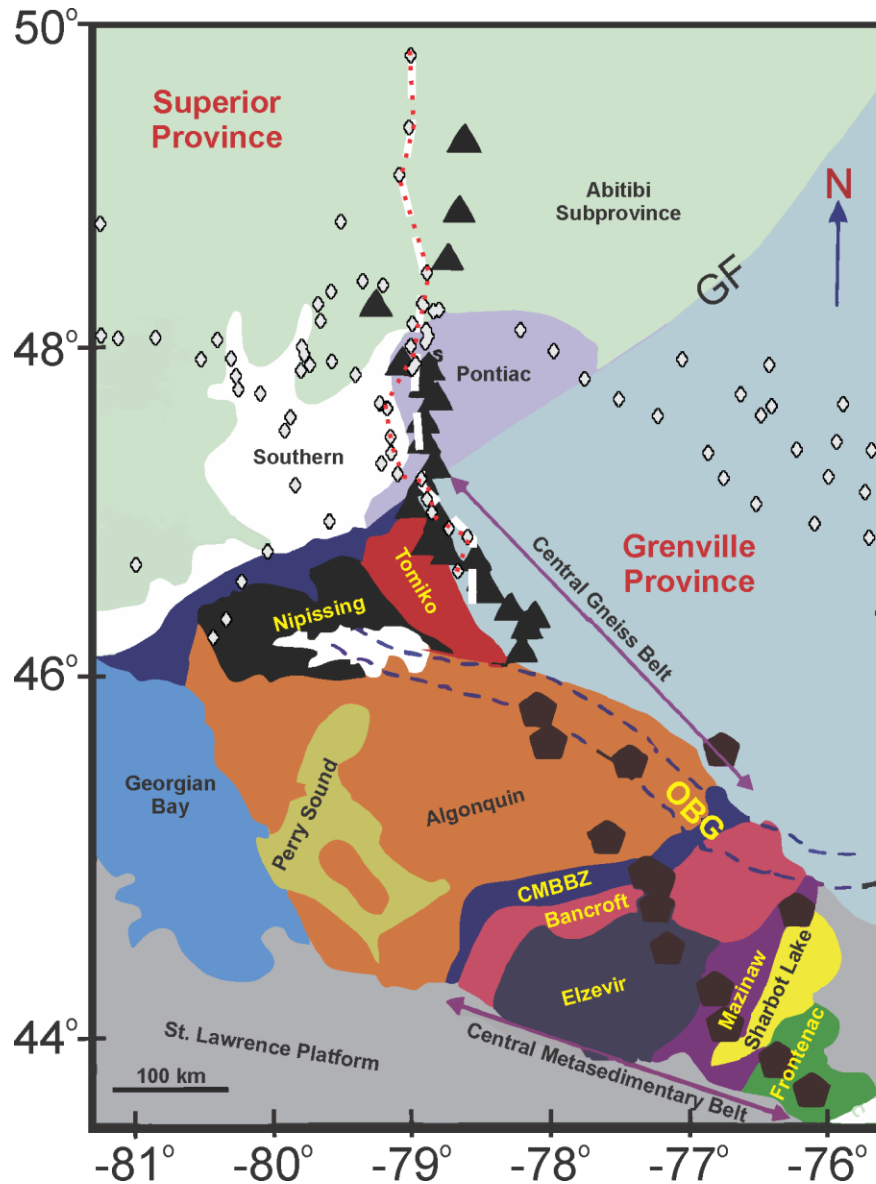

Figure 13: Simplified geotectonic map of the study area showing the location of the MT sites. Black triangles and pentagons represent MT sites from the Lithoprobe and POLARIS projects, respectively. Grey diamonds represent a subset of the sites used in this study. White dashed line indicates the path of the slice from the 3-D model given in Figure 12 and 13. Red dotted line indicates the path of the Niblett-Bostick section shown in Figure 15. Modified after Adetunji et al. (2014).

Figure 14 shows a comparison of the crustal and lithospheric resistivity models from the 2-D inversion of Adetunji et al. (2014) and a compilation of the 3-D models generated for this study. Note that the 2-D model in Figure 14 has been truncated at the south-east end to match the 3-D model. At first glance, the models are remarkably similar. Both models have resistive upper crusts with thickness ranging from 10 to 20 km and resistivities greater than 10000 Ω-m (R1a and R1b), exhibit generally increasing conductivity with increasing depth, and have conductive anomalies with resistivities of ~10 Ω-m between 60-130 km depth (C2c). Furthermore, both models have conductive features in the lower crust (C2b), extending approximately 40 km to the south-east and abruptly transitioning into resistive feature (R1b). While the labelled features are found in some form in both models, the locations of most of the features is different between the 2-D and 3-D inversions. In the 3-D model C2b and C2c occur near a latitude of 48˚, which corresponds to the boundary between the Abitibi and Pontiac sub-provinces, whereas the similar features found in the 2-D models are found close to 47˚ latitude at the boundary between the Pontiac sub-province and the beginning of the Central Gneiss Belt (CGB). This boundary is also known as the Grenville Front (GF). Both models show resistive features (R2), denoted in Adetunji et al. (2014) as a 'modified Archean lithosphere'. In the 2-D model, this feature begins 50 km depth directly to the south of the GF, and dips further to the south-east for ~300 km (not shown). A similar feature is evident in the 3-D model, however it begins ~50 km north-east of the GF and terminates within ~100 km, although this likely has more to do with the lack of sites (and therefore lack of sensitivity) to the south of the GF than the data itself. As with most of the deeper resistive features in the 3-D model, feature R2 is not well resolved according to the calculated resolution matrix.
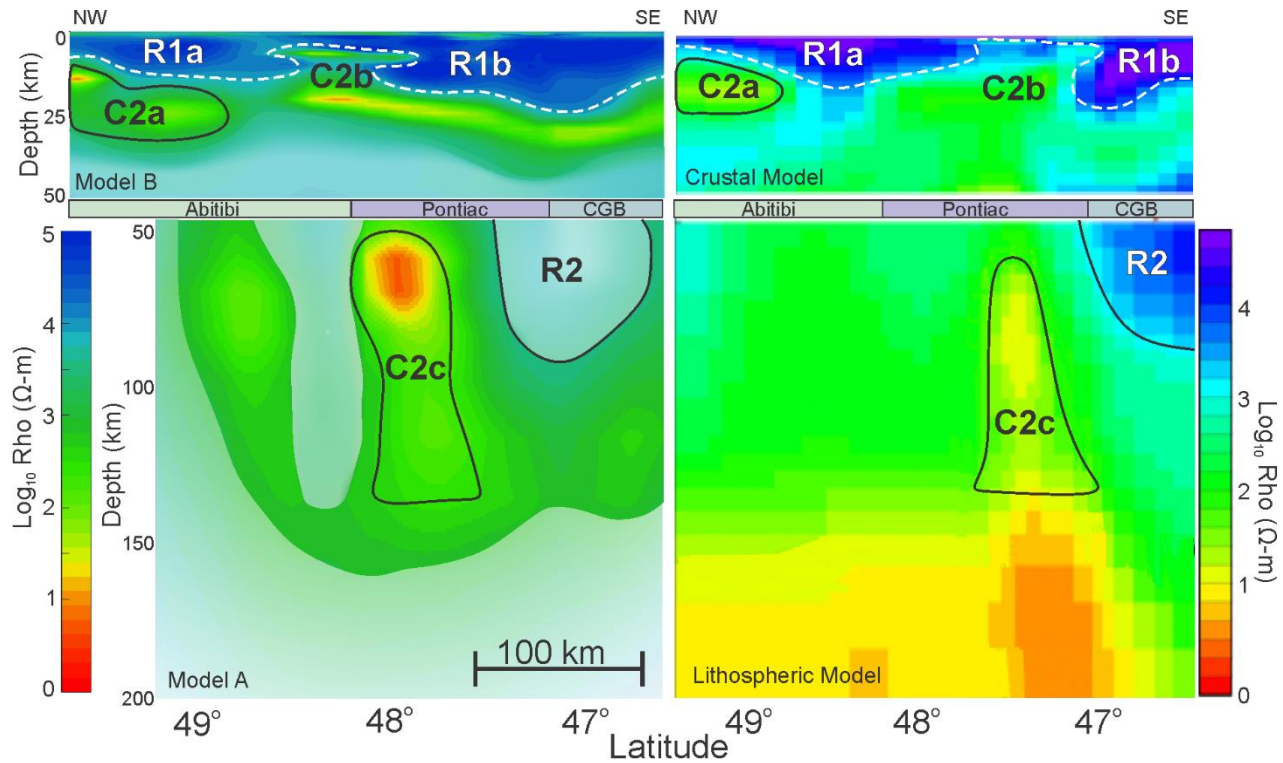
Figure 14: Crustal and lithospheric models from the 3-D (left) and 2-D (right) inversions. The slices of the 3-D model are the same as those shown in Figure 12, while the 2-D model is that presented in Adetunji et al. (2014). Transparency in the 3-D model indicates areas with lower than average resolution.

A sensitivity test was performed over the uppermost portion of conductor C2c in order to help determine if it is required by the data. Using the focused 3-D model, a block with a resistivity of 10000 Ω-m was placed over C2c at depths between 5 and 15 km, and the forward model was calculated. Overall, the RMS increased by only 0.24 (going from an RMS of 2.56 to 2.8), however, the RMS for sites in the immediate vicinity of C2c increased by an average of 0.92. The increase in RMS misfit at these sites suggests that some sort of conductive feature is likely required near the boundaries between the Abitibi, Pontiac, and Southern sub-provinces.

A closer look at the data in the form of a Niblett-Bostick transform of the determinant average resistivities is shown in Figure 15. The plot shows an interpolated slice through the Niblett-Bostick transformed determinant-average data along a similar profile taken in Figure 14. In order to limit the amount of interpolation, the slice was taken moving between each site along the profile. The difference in the paths taken by the profiles is for the most part negligible; however, there is a slight shift to the west near the center of the Niblett-Bostick profile which means the portion of the plot near latitude 47° will coincide with the boundary between the Southern and Pontiac rather than the GF.
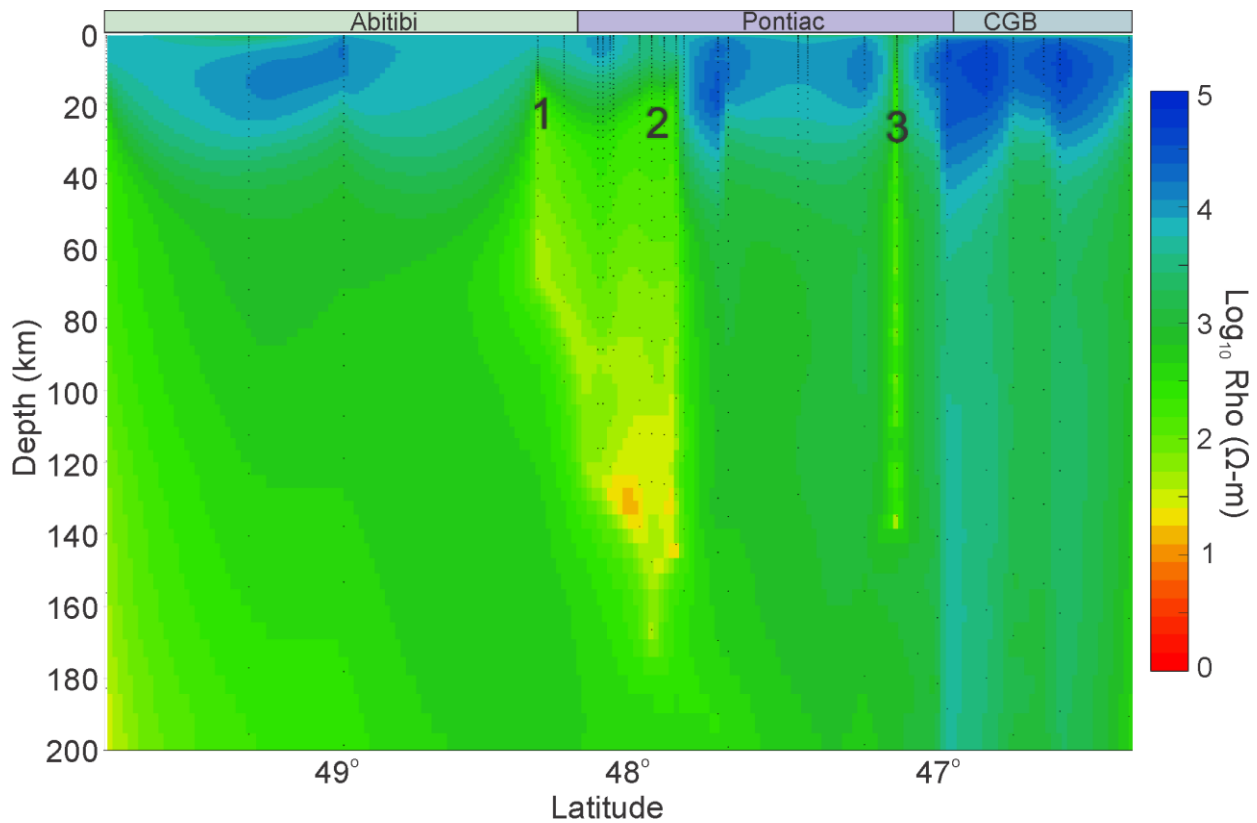
Figure 15: Interpolated slice through Niblett-Bostick transformed of the determinant average resistivities data along the sites nearest to the profile indicated by the dashed line Figure 13. Dots indicate available data points.

As in the 2-D and 3-D models, the transformed data indicates a generally resistive crust to depths of at least 20 km. However, it also shows three regions with increased conductivity at depths less than 20 km. Two of these regions coincide with bounds of feature C2c as seen in the 3-D model, around the northern portion of the boundaries between the Abitibi and Pontiac sub-provinces. The third region coincides with the southeastern edge of boundary between the Southern and Pontiac. This seems to suggest that most of the conductivity seen in the models at crustal depths is due to conductors within or at the boundaries of the Southern and Pontiac, as well near the southern edge of the Abitibi sub-province.

Acknowledgments

References

Adetunji, A.Q., Ferguson, I.J., Jones, A.G., 2014. Tectonophysics Crustal and lithospheric scale structures of the Precambrian Superior – Grenville margin. Tectonophysics 614, 146–169. doi:10.1016/j.tecto.2013.12.008

Alumbaugh, D.L., Newman, G. a., 2000. Image appraisal for 2-D and 3-D electromagnetic inversion. Geophysics 65, 1455–1467. doi:10.1190/1.1444834

Björk, Å., 1996. Numerical Methods for Least Squares Problems. SIAM, Philadelpia.

Boerner, D.E., Kurtz, R.D., Craven, J.A., 2000. A summary of electromagnetic studies on the Abitibi– Grenville transect. Can. J. Earth Sci. 37, 427–437.

Cagniard, L., 1953. Basic theory of the magnetotelluricmethod of geophysical prospecting. Geophysics 18, 605–635.

Card, K.D., 1990. A review of the Superior Province of the Canadian shield, a product of Archean accretion. Precambrian Res. 48, 99–156.

Card, K.D., Ciesielski, A., 1986. Subdivisions of the Superior Province of the Canadian Shield. Geosci. Can. 13, 5–13.

Card, K.D., Poulsen, K.H., 1998. Geology and mineral deposits of the Superior Province of the Canadian shield. In: Lucas, S.B. (Ed.), Geology of the Precambrian Superior and Grenville Provinces and Precambrian Fossils in North America. Geology of Canada Series, No. 7. Geological Survey of Canada, pp. 13–194.

Chave, A.D., Jones, A.G. (Eds.), 2012. The Magnetotelluric Method — Theory and Practice. Cambridge University Press, New York (570 pp.).

Constable, S.C., 2006. SEO3: a new model of olivine electrical conductivity. Geophys. J. Int. 166, 435–437.

Glover, P.W.J., Vine, F.J., 1995. Beyond KTB — electrical conductivity of the deep continental crust. Surv. Geophys. 16, 5–36.

Ducea, M.N., Park, S.K., 2000. Enhanced mantle conductivity from sulfide minerals, southern Sierra Nevada, California. Geophys. Res. Lett. 27, 2405–2408.

Evans, R.L., Jones, A.G., Garcia, X.,Muller,M., Hamilton,M., Evans, S., Fourie, C.J.S., Spratt, J., Webb, S., Jelsma, H., Hutchins, D., 2011. Electrical lithosphere beneath the Kaapvaal craton, southern Africa. J. Geophys. Res. 116, B04105.

Ferguson, I.J., Jones, A.G., Chave, A.D., 2012. Case histories and geological applications. In: Chave, A.D., Jones, A.G. (Eds.), The Magnetotelluric Method: Theory and Practice. Cambridge University Press, New York, pp. 480–544.

Grayver, A.V., 2013. Three-dimensional controlled-source electromagnetic inversion using modern computational concepts.

Hirth, G., Evans, R.L., Chave, A.D., 2000. Comparison of continental and oceanic mantle electrical conductivity: is the Archean lithosphere dry? Geochem. Geophys. Geosyst. 1, 1030. http://dx.doi.org/10.1029/2000GC000048.

Hoffman, P.F., 1989. Precambrian geology and tectonic history of North America. In: Bally, A.W., Palmer, A.R. (Eds.), The geology of North America —An Overview. The Geological Society of America, vol. A, pp. 447–512.

Hyndman, R.D.,Wang, K., Yuan, T., Spence, G.D., 1993. Tectonic sediment thickening, fluid expulsion, and the thermal regime of subduction zone accretionary prisms: the Cascadia margin off Vancouver Island. J. Geophys. Res. 98, 21865–21876. http:// dx.doi.org/10.1029/93JB02391

Jones, A.G., 1999. Imaging the continental upper mantle using electromagnetic methods. Lithos 48, 57–80.

Jones, A.G., Craven, J.A., 2004. Area selection for diamond exploration using deep-probing electromagnetic surveying. Lithos 77, 765–782.

Karato, S., 1990. The role of hydrogen in the electrical conductivity of the upper mantle. Nature 347, 272–273.

Katsube, T.J., Mareschal, M., 1993. Petrophysical model of deep electrical conductors: graphite lining as a source and its disconnection due to uplift. J. Geophys. Res. 98, 8019–8083.

Kiyan, D., Jones, A.G., Vozar, J., 2014. The inability of magnetotelluric off-diagonal impedance tensor elements to sense oblique conductors in three-dimensional inversion. Geophysical Journal International 196, 1351–1364. doi:10.1093/gji/ggt470

Korja, T., 2007. How is the European lithosphere imaged by magnetotellurics? Surv. Geophys. 28, 239–272.

Li, S., Unsworth, M.J., Booker, J.B., Wei, W., Tan, H., Jones, A.G., 2003. Partial melt or aqueous fluid in the mid-crust of Southern Tibet? Constraints from INDEPTH Magnetotelluric data. Geophysics 153, 289–304.

Percival, J.A., Bleeker, W., Cook, F.A., Rivers, T., Ross, G., van Staal, C., 2004. PanLITHOPROBE Workshop IV: intra-orogen correlations and comparative orogenic anatomy. Geosci. Can. 31, 23–39.

Selway, K., 2013. On the causes of electrical conductivity anomalies in tectonically stable lithosphere. Surv. Geophys.. http://dx.doi.org/10.1007/s10712-013-9235-1.

Sibson, R., 1981. A brief description of natural neighbor interpolation, in: Barnett, V. (Ed.), Interpreting Multivariate Data. Wiley, New York, pp. 21–36.

Siripunvaraporn, W., Egbert, G., Lenbury, Y., Uyeshima, M., 2005. Three-dimensional magnetotelluric inversion: Data-space method. Physics of the Earth and Planetary Interiors 150, 3–14. doi:10.1016/j.pepi.2004.08.023

Smith, J.T., Booker, J.R., 1988. Magnetotelluric inversion for minimum structure. Geophysics 53, 1565–1576. doi:10.1190/1.1442438

Spratt, J.E., Jones, A.G., Jackson, V.A., Collins, L., Avdeeva, A., 2009. Lithospheric geometry of the Wopmay orogen from a Slave craton to Bear Province magnetotelluric transect. J. Geophys. Res. 114, B01101.

Tikhonov, A.N., 1950. The determination of the electrical properties of the deep layers of the Earth's crust. Dokl. Acad. Nauk SSR 73, 295–297 (in Russian).

Appendix
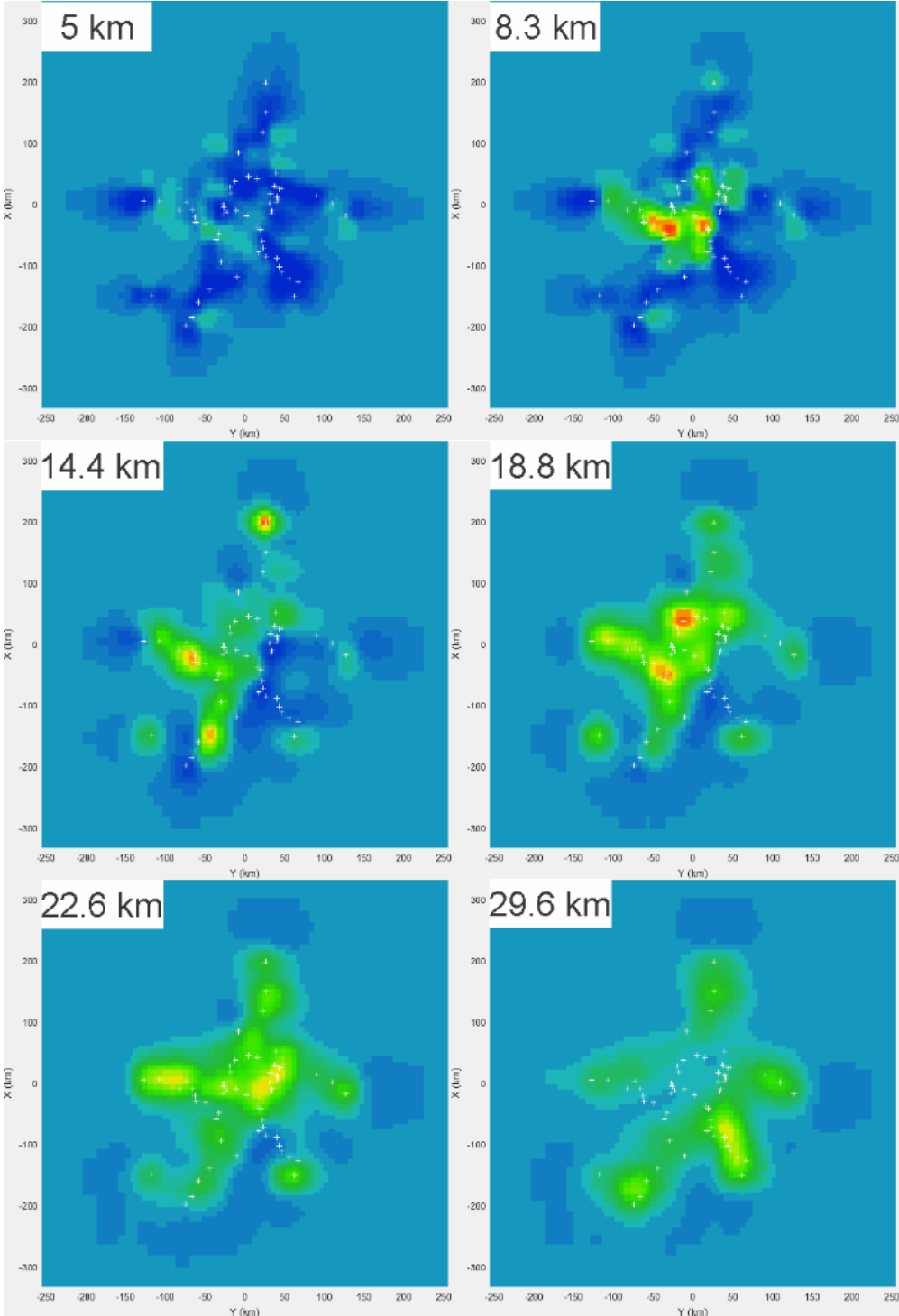
Plan view of the focused model (Model B) at various depths.
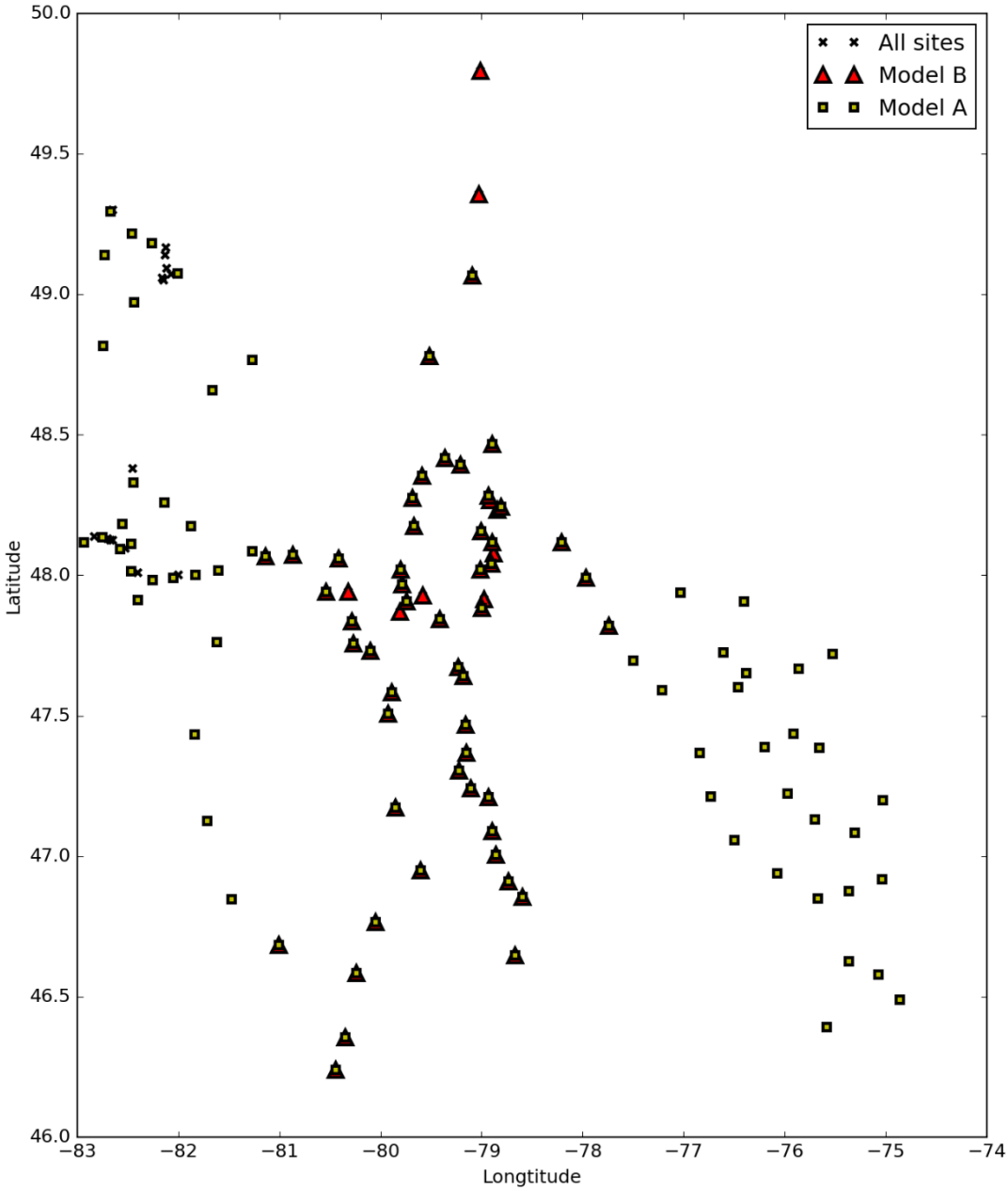
Station locations for the Abitibi-Grenville survey